Nano Energy 62 (2019) 79–84

Contents lists available at ScienceDirect

Nano Energy

journal homepage: www.elsevier.com/locate/nanoen

Communication

Built-in oriented electric field facilitating durable Zn−MnO_2 battery

Sitian Lian[a], Congli Sun[a], Weina Xu[b,c,d], Wangchen Huo[d], Yanzhu Luo[e], Kangning Zhao[a,b,*], Guang Yao[c], Wangwang Xu[f], Yuxin Zhang[d], Zhi Li[a], Kesong Yu[a], Hongbin Zhao[b], Hongwei Cheng[b,c], Jiujun Zhang[b], Liqiang Mai[a,**]

[a] States State Key Laboratory of Advanced Technology for Materials Synthesis and Processing, Wuhan University of Technology, Wuhan, 430070, PR China
[b] College of Sciences & Institute for Sustainable Energy, Shanghai University, Shanghai, 200444, China
[c] Department of Material Science and Engineering, University of Wisconsin-Madison, Madison, WI, 53706, USA
[d] College of Materials Science and Engineering, Chongqing University, Chongqing, 400044, China
[e] College of Science, Huazhong Agricultural University, Wuhan, 430070, China
[f] Department of Mechanical and Industrial Engineering, Louisiana State University, Baton Rouge, LA, USA

ARTICLE INFO

Keywords:
Oxygen vacancy
Ti doping
Localized electric field
Zn ion battery

ABSTRACT

Rechargeable aqueous zinc ion batteries are particularly attractive for large-scale application due to their features including low cost, environmental friendliness, and safety. Herein, we report the use of defect engineering to generate oxygen vacancies in tunneled α-MnO_2 through surface gradient Ti doping for long-life Zn−MnO_2 battery. Interestingly, the introduction of surface gradient Ti doping leads to shrinkage of the interlayer, but simultaneously generates oxygen vacancies as compensated by electron due to the decreased valence state of Mn. Moreover, Ti substitution as well as the created oxygen vacancies open the [MnO_6] octahedral walls and result in imbalanced charge distribution and local electric field in the crystal structure, accelerating ion/electron migration rates. Thus, diffusion coefficients of both Zn^{2+} and H^+ ions in Ti−MnO_2 nanowires are improved. Consequently, the Ti−MnO_2 nanowires show improved both H^+ and Zn^{2+} ions storage capacity in Zn/MnO_2 battery and achieved excellent high-rate capability and ultralong cycling stability with a low capacity decay rate of 0.005% per cycle at high rate of 1 A g^{-1}. It is believed that the intentionally created vacancies in this work opens up approaches to enhance existing materials that may have applications in more efficient and durable multi-valent ion battery and other technologies.

1. Introduction

Recently, multivalent-ion batteries have received considerable attentions due to the potential stationary storage systems, as renewable energy technologies are penetrating towards large scale [1–12]. Although the di/tri-valent metal ion batteries, such as Mg, Al, Zn, etc, have rather lower mass capacities and higher reduction potentials compared to lithium, the low cost and high volumetrical capacity make them good competitors in application of grid energy storage devices, again Li ion battery [13–19]. Among those, zinc is globally abundant with a high theoretical capacity (820 mAh g^{-1}) and a high energy density (5851 mAh mL^{-1}) and shows suitable negative potential (−0.762 V *vs.* SHE) as well as high overpotential against hydrogen evolution [20–30]. These advantages make zinc very suitable as anode for aqueous battery. Additionally, the ability of Zn^{2+} ion to transfer two electrons enables a large storage capacity, compared with Li/Na ion battery in which only one electron is transferred per atom [25,26,31]. In this regard, aqueous rechargeable zinc ion battery (ARZIB) is promising in application for grid energy storage devices [24,29,31].

However, compared with Li^+ ion intercalation chemistry, due to the strong electrostatic interactions with the host lattice of divalent Zn^{2+} ions, zinc ion host often shows slow Zn^{2+} diffusion rate and limited reversibility [32–34]. Thus, most electrode materials that can accommodate Li^+ ions insertion/extraction are not suitable for ARZIBs. Among those, Mn-based cathodes deliver higher energy density than that of other kinds of cathodes (including vanadium-based oxides [22,32,33], Prussian blue analogs [35]). However, they are suffering from the dissolution of Mn and structural degradation, which results in the significant capacity fading [36]. Up to date, various MnO_2 of different polymorphs have been investigated but have eventually reached

* Corresponding author. States State Key Laboratory of Advanced Technology for Materials Synthesis and Processing, Wuhan University of Technology, Wuhan, 430070, PR China.
** Corresponding author.
E-mail addresses: vicyel@126.com (K. Zhao), mlq518@whut.edu.cn (L. Mai).

https://doi.org/10.1016/j.nanoen.2019.04.038
Received 21 February 2019; Received in revised form 8 April 2019; Accepted 8 April 2019
Available online 25 April 2019

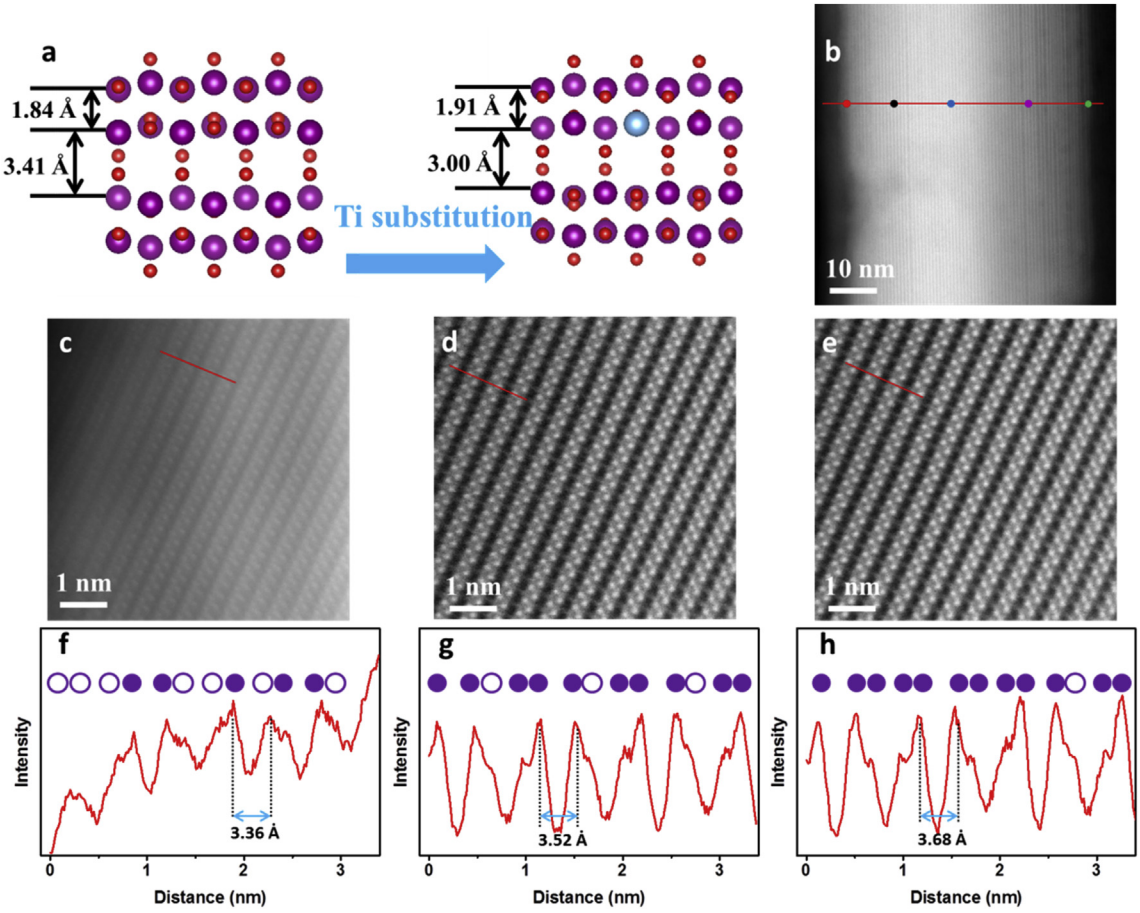

Fig. 1. Relative surface composition changes for the Ti−MnO_2 NWs. a, the calculated tunnel structure of pristine and Ti-doped α-MnO_2. **b,** STEM image of Ti−MnO_2. HRSTEM images of **c,** surface area, **d,** mid-surface area, and **e,** middle area of a single Ti−MnO_2 NW and the corresponding line profiles crossing the Mn layer in the **f,** surface area, **g,** mid-surface area, and **h,** middle area.

a bottleneck. Consequently, vacancies could effectively adjust the electronic structure without radically changing the pristine lattice, and unlock potential for optimizing the performance of multi-valent ions storage [37–42]. For instance, recently, Dambournet and his colleague reported the boosting di/tri-valent ion (Mg^{2+} and Al^{3+}) storage through rational introduction of a large number of titanium vacancies as intercalation sites [43,44]. Thus, it is highly expected that rational introduction of defects can boost the di-valent Zn^{2+} ion storage performance. Previous study indicates that the introduction of Ag^{+} in the α-MnO_2 would result in oxygen vacancy [45]. Hence, it is expected that the introduction of metal dopant in the tunnel wall would be beneficial of creating oxygen vacancy.

Herein, we report the tunneled α-MnO_2 through rationally surface gradient Ti doping to generate oxygen vacancies in (denoted as Ti−MnO_2) for zinc ion battery. Interestingly, the introduction of surface gradient Ti doping leads to shrinkage of the interlayer, and simultaneously generates surface gradient oxygen vacancies as compensated by electron due to the decreased valence state of Mn. The Ti substitution, as well as the created oxygen vacancies, open the [MnO_6] octahedral walls, leading to imbalanced charge distribution and localized electric field, which accelerates ion/electron migration rates and promote charge transfer behavior of both H^{+} and Zn^{2+} ions, which is confirmed both experimentally and theoretically. Consequently, benefiting from the unique gradient structure, the Ti−MnO_2 NWs show improved both H^{+} and Zn^{2+} ions storage capacity in Zn/MnO_2 battery and achieved excellent high-rate capability and ultralong cycling stability with a low capacity decay rate of 0.005% per cycle at high rate of 1 A g^{-1}. It is believed that the intentionally created vacancies in this work will provide further insights into the design of other electrodes for multi-valent ion battery.

2. Results and discussion

The Ti−MnO_2 NWs is obtained through the solid diffusion of the ALD grown TiO_2 into the MnO_2 NW body (Fig. S1). Because of the substantial difference in Fermi level between Ti^{4+} and Mn^{4+}, substituting a small number of Mn^{4+} with Ti^{4+} is effective for preventing charge ordering and decreasing the electronic localization [44,46]. Density functional theory (DFT) calculations in Fig. 1a predicts that contraction of tunnel in MnO_2 after Ti substituting Mn site. The typical transmission electron microscopic (TEM) image in Fig. S2 shows the one-dimensional morphology of the Ti−MnO_2. The high-angle annular dark field (HAADF) scanning TEM (STEM) images of the MnO_2 recorded along [001] zone axes in Fig. 1b. The contrast of the STEM image exhibits dependence with respect to the atomic number Z. Thus, the brighter dots represent the heavier atomic columns (Ti and Mn), while the O atoms are invisible in the HAADF image, as they are not heavy enough to produce any contrast [47]. The atomic arrangement revealed in the HAADF STEM image is identical to the atomic configuration viewed along [001] orientation, showing the tunnel structure of α-MnO_2 (Fig. 1a). The large one-dimensional tunnel formed by [MnO_6] polyhedrons can be clearly seen. No intergrowth of tunnel heterogeneity is observed [48]. The high-resolution scanning transmission electron microscopic (HRSTEM) images of the NW body in different area are captured. The tunneled structures of the NW in the surface, mid-surface, and middle area are well retained after Ti doping. No

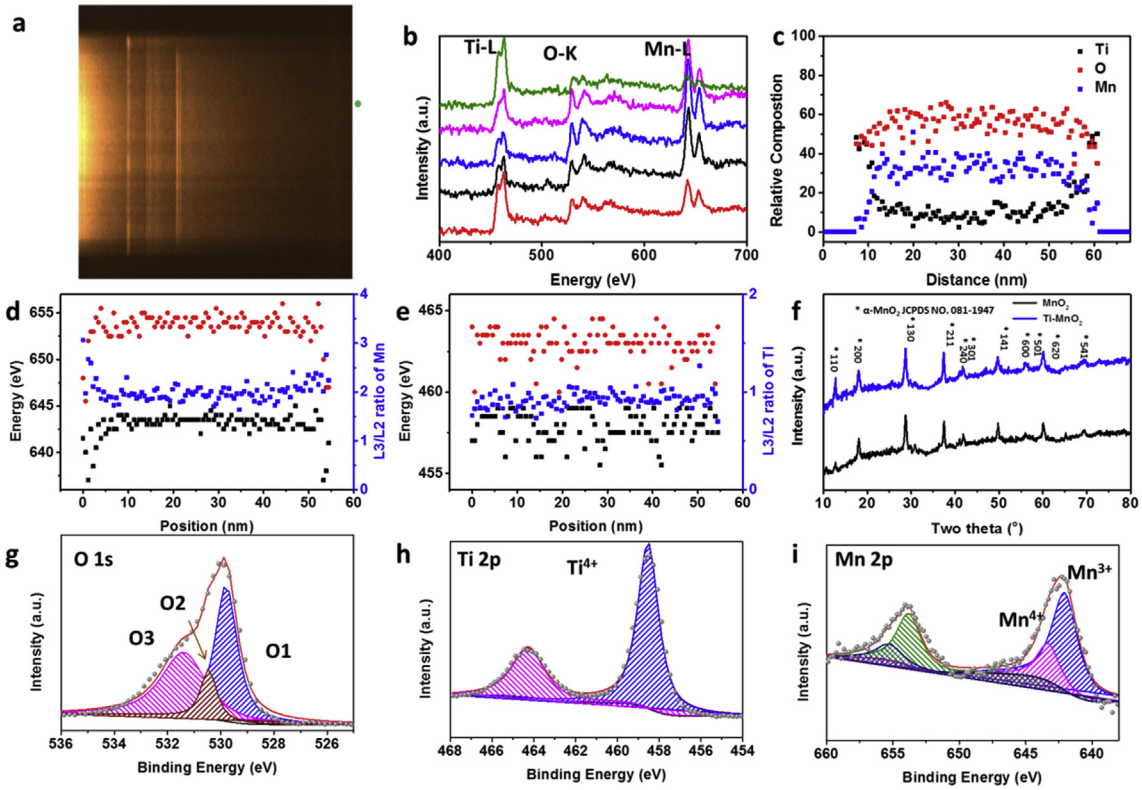

Fig. 2. Structural characterizations for the Ti−MnO_2 NWs. a, EELS spectrum image of selected area from the vertical red line in the left STEM image in Fig. 1b, showing O K, Mn $L_{2,3}$, Ti $L_{2,3}$ edges. **b,** EELS spectrum profiles from the surface to the interior as marked by the horizontal dashed lines with the same color as in Fig. 1b **c,** Relative atomic composition of O (red), Mn (blue), and Ti (black) as a function of position calculated based on the integrated EELS peak intensity in **b**. **d,** Energies of Mn L_3 (black) and L_2 (red) edges, as well as intensity ratio of L_3/L_2 (blue) from the EELS spectrum image. **e,** Energies of Ti L_3 (black) and L_2 (red) edges, as well as intensity ratio of L_3/L_2 (blue) from the EELS spectrum image. **f,** XRD patterns of Ti−MnO_2 NWs and MnO_2 NWs. **g-i,** high-resolution XPS spectrum of O 1s, Ti 2p, and Mn 2p in Ti−MnO_2 NWs.

obvious contrasts were observed in the tunnel, wiping out the possibility of Ti intercalated into the tunnel structure. Line profiles crossing the tunnel structure are captured in the surface area, mid-surface and middle area, are shown in Fig. 1c, d, and 1e. By comparing the repeat units in Fig. 1f, g, and 1h, a subtle change in the tunnel diameter is captured and the tunnel diameter gradually increases from 3.36 to 3.68 Å. Additionally, the variation in atomic column intensity observed on the high-resolution image (Fig. 1a) corresponds to a variation in the Mn atomic occupation, and hence, points to the presence of possible Ti substitution site. Thus, atoms with large Z will emerge and hence, the Mn site which is substituted by Ti will exhibit the lower intensity. The possible substitution site is highlighted by the empty slot in upper side of Fig. 1f, g, and 1h. More empty slots are observed in the surface while the number decreases in the mid-surface and middle area, suggesting that there are more Ti atoms in the surface and possibly leading to a surface gradient Ti doping MnO_2 NW structure. The TiO_2@MnO_2 NWs shows that the thickness of the shell is ~5 nm and the FFT pattern of the shell confirms that the TiO_2 shell is amorphous in Fig. S2. After annealing, the FFT pattern of the shell in Fig. S3 becomes obvious and identical with the core, suggesting that Ti dopes into the MnO_2 NW. MnO_2 NW is also conducted as a comparison and no concentration gradient is observed in Fig. S4.

The Ti and Mn site preferences were further examined by atomic-scale STEM-electron energy loss spectrum (EELS) to study relative surface composition and chemical state of Ti−MnO_2 NWs. EELS line scan was collected at different positions from bulk to surface as shown in Fig. 2a. By integrating the intensity of the O, Ti and Mn peaks, the relative composition can be obtained in Fig. 2b. Interestingly, O K edge pre-peak intensities are quite low on both surface sides. The reduced ratio of the O K edge pre-peak intensities to the main peak can result from a change in the local environment of oxygen, especially from the oxygen vacancies formed on the surface. The relative distribution of chemical composition of Mn, Ti, and O elements are plotted in Fig. 2c. The oxygen ratio gradually increases from 45% in the surface and become stabilized at ~55% from 10 nm towards the middle area. The lowered oxygen ration in the surface suggests the formation of oxygen vacancy. Furthermore, the Mn $L_{3,2}$ and Ti $L_{3,2}$ edges are plotted along the NW in Fig. 2d and e, respectively. The energies of the Mn $L_{3,2}$ edges are lower in the surface region (~10 nm). Moreover, the intensity ratio of Mn L_3/Mn L_2 is ~3 in the surface region and tapered off to ~2.6 in the middle area. This suggests that the valence of Mn is lower in the surface. On the contrast, the energies of the Ti $L_{3,2}$ edges are the same in the whole NW and the intensity ratio of Ti L_3/Ti L_2 stabilizes at ~0.8 in both surface and middle region, suggesting the valance state of Ti in the NW body is +4. Combined with the composition ratio with the valence state, it is believed that the doped Ti is expected to donate electrons, thus reducing the valence of Mn and leading to the formation of oxygen vacancy [45]. The XRD is carried out in Fig. 2f. The XRD patterns of MnO_2 and Ti−MnO_2 show similar patterns and correspond well with α-MnO_2 (JCPDS NO. 081–1947). It is found that the (200) peak shift towards high angle (Fig. S4), suggesting the contraction of the tunnel, which is consensus with the STEM results. To further identify the oxygen vacancy in the Ti−MnO_2, XPS is carried out in Fig. 2g, **h**, and **2i**. The O1s spectrum in Fig. 2g shows three oxygen peaks. O1 at 529.8 eV is typical for metal-oxygen bonds, O2 at 531.4 eV for the oxygen in OH− groups, whereas O3 at the higher value of 532.0 eV attributed to the high-binding energy peak from surface oxygen defect species [49], which also confirms the formation of oxygen vacancy in the surface area [50]. In Mn 2p spectrum (Fig. 2i), two peaks contribute to the total spectrum, which suggests the co-

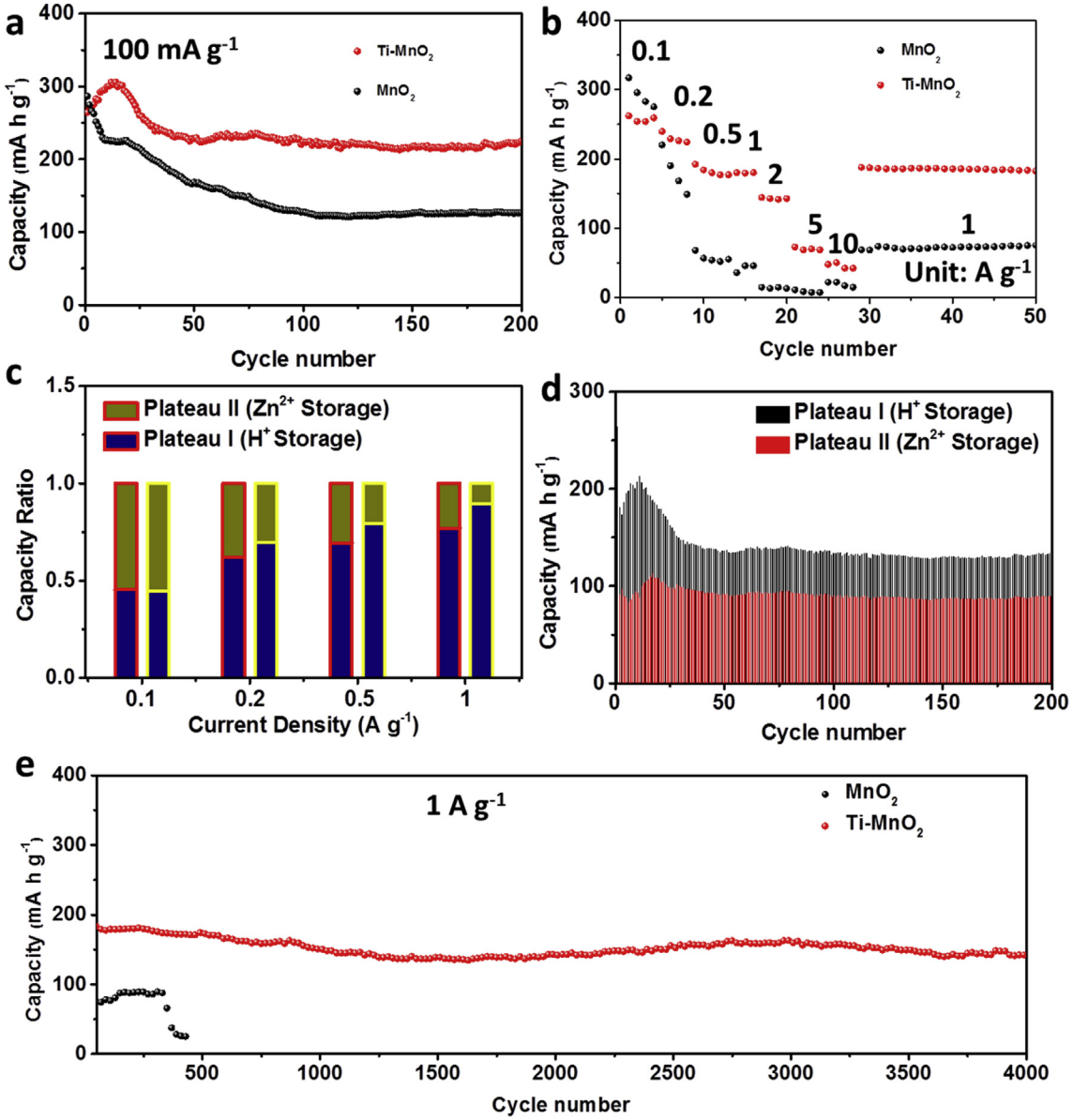

Fig. 3. Electrochemical performance for the Ti−MnO_2 NWs. a, Cycling performance of Ti−MnO_2 NWs and MnO_2 NWs at 100 mA g^{-1} **b,** rate capabilities of Ti−MnO_2 NWs and MnO_2 NWs. **c,** separation of H^+ and Zn^{2+} storage capacity at different rate. **d,** reversible (discharge) capacity *vs.* cycle number separated from Plateau I (H^+ storage) and Plateau II (Zn^{2+} storage). **e,** cyclic performance at 1 A g^{-1} of Ti−MnO_2 NWs and MnO_2 NWs.

existence of Mn^{3+} and Mn^{4+}. It is very interesting to see that the peak of Mn^{3+} occupies 64% of the total area, further confirming the decreased valence state of Mn, which is consensus to the EELS results in Fig. 2e. In Ti 2p spectrum (Fig. 2h), only one peak is observed, indicating that the valence of Ti is +4, which is also consensus with the result of EELS in Fig. 2e. All these results indicate that the oxygen vacancies are formed through Ti doping and the oxygen vacancy is rich in the surface region, leading to a concentration gradient in the NW body.

The electrochemical performance of Zn/MnO_2 battery by utilizing Ti−MnO_2 NWs as cathode were investigated using coin cells employing Zn foil as anode, 3 M $Zn(CF_3SO_3)_2$ and 0.1 M $Mn(CF_3SO_3)_2$ aqueous mixture as electrolyte [29], and glassy fiber as separator. Fig. 3a shows the cycling performance of Ti−MnO_2 NWs and MnO_2 NWs at 100 mA g^{-1}. Ti−MnO_2 NWs show reversible capacity up to 225 mAh g^{-1} after 200 cycles, approaching the theoretical value of MnO_2 (308 mAh/g based on single electron transfer between Mn^{4+}/Mn^{3+} redox pair). On the contrast, a reversible capacity of only 126 mAh g^{-1} is retained for MnO_2 NWs. Furthermore, the rate performance is also evaluated at different current densities ranging from 0.1 to 10 A g^{-1} in Fig. 3b. The Ti−MnO_2 NWs deliver capacities of 259, 229, 180, 179, 142, 72, and 50 mAh g^{-1}. The Ti−MnO_2 shows much higher capacities at high rates. The charge and discharge curves of Ti−MnO_2 NWs under various current densities are shown in Fig. 3c, from which obvious charge and discharge plateaus can be discerned. The turning point can be obviously observed when current density is below 1 A g^{-1}. According to the previous report [31] and the electrochemical performance without $Zn(CF_3SO_3)_2$ in Fig. S8, the discharge curves can be divided into two parts based on the turning point, namely, H^+ insertion (Plateau I) at higher voltage and Zn^{2+} intercalation (Plateau II) at lower voltage (Fig. S6). In this way, we can divide the capacity into H^+ storage capacity and Zn^{2+} storage capacity according to the turning point, as shown in Fig. S7. At low current density of 0.1 A g^{-1}, the Zn^{2+} storage capacity ratio of Ti−MnO_2 NWs is slightly lower than that of MnO_2 NWs. The Zn^{2+} storage capacity ratio gradually decreases with the increasing of the current density, which may be due to the sluggish diffusion rate of Zn^{2+} ions compared with H^+ ions. More specifically,

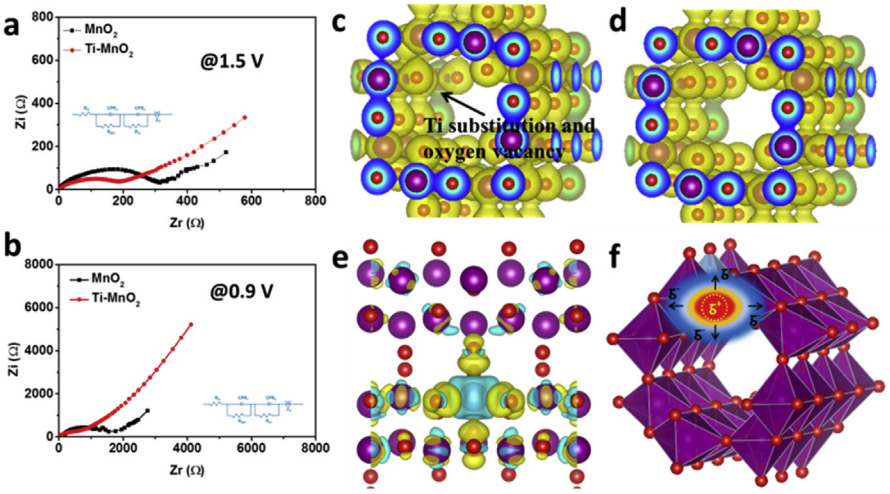

Fig. 4. The electronic structure calculations of the Ti−MnO_2. EIS spectrum of **a,** MnO_2 NWs and **b,** Ti−MnO_2 NWs. Charge density distribution of **c,** Ti−MnO_2 and **d,** MnO_2. **e,** Charge density differences of Ti−MnO_2 and MnO_2. Yellow and blue regions indicate electron accumulation and depletion zones, respectively. **f,** schematic illustration of corresponding charge transfer behavior upon charging/discharging.

at 1 A g^{-1}, 23% capacity of Ti−MnO_2 NWs is still contributed from Zn^{2+} storage compared with only 10% capacity of MnO_2 NWs from Zn^{2+}, suggesting an improved Zn^{2+} storage capacity contribution after Ti doping. We further quantify capacity contributed from H^+ and Zn^{2+} based on the cycling performance at 100 mA g^{-1} in Fig. 3d. The Zn^{2+} storage of Ti−MnO_2 NWs contributes a very stable capacity of ~100 mAh g^{-1} throughout the cycles. On contrast, MnO_2 shows similar trends in the initial cycles as shown in Fig. S9. During the capacity fading process, both H^+ and Zn^{2+} storage capacities decay in the initial 50 cycles. After then, the H^+ storage capacities stabilize at ~110 mAh g^{-1} while the Zn^{2+} storage capacities keep on decreasing to ~28 mAh g^{-1}. These results suggest that the capacity fading is mainly ascribed to the decreased zinc storage capacity while the H^+ storage capacity remains constant. Thus, it can be concluded that Ti−MnO_2 NWs is more stable in accommodating Zn^{2+} ions intercalation/de-intercalation, as zinc ions show more sluggish kinetic. The long term cycling performance at 1A g^{-1} is also evaluated in Fig. 3e and outstandingly, the Ti−MnO_2 NWs shows a low capacity decay rate of 0.005% per cycle after 4000 cycles, demonstrating the excellent long-term cycling performance. To further to investigate the influence of Ti doping on the H^+ and Zn^{2+} storage performance, EIS spectrum at different voltages, typically, at 1.5 and 0.9 V, which correspond to Plateau I (H^+ storage) and Plateau II (Zn^{2+} storage), respectively, are evaluated in Fig. 4a and b, respectively. All the spectra exhibited a compressed semicircle correlated to the charge transfer resistance (R_{ct}, high frequency) and an inclined line (ω, low frequency). At 1.5 V, the EIS spectrum of Ti−MnO_2 shows both smaller charge transfer resistance and Warburg impedance, compared with those of pristine MnO_2. The values of diffusion coefficients of H^+ and Zn^{2+} can be calculated from the inclined lines in the Warburg region using the following equation:

$$D = R^2T^2/2A^2n^4F^4C^2\delta^2$$

in which T is the absolute temperature, A is the surface area of the cathode electrode, n is the number of electrons per molecule during oxidization, F is the Faraday constant, C is the ion concentration, and δ is the Warburg factor associated with Z_{re} ($Z_{re} \propto \delta\omega^{1/2}$). Based Warburg factor at 1.5 V, the apparent diffusion coefficients of H^+ in Ti−MnO_2 and MnO_2 are 8.5×10^{-13}, and 3.1×10^{-13} $cm^2 s^{-2}$. On the contrast, the EIS spectrum at 0.9 V shows much lower charge transfer and diffusion resistance in Fig. S8, compared with those at 1.5 V, further confirming the sluggish kinetics of Zn^{2+}. By calculating the Warburg factor at 0.9 V, the apparent diffusion coefficients of Zn^{2+} in Ti−MnO_2 and MnO_2 are 5.0×10^{-15} and 3.6×10^{-15} $cm^2 s^{-2}$, respectively. Thus, it can be concluded that Ti-MnO_2 shows improved kinetics in both H^+ and Zn^{2+} storage, which is critical in improving the electrochemical performance.

The morphology and structure after long-term cycling were also investigated through TEM, STEM, and XPS. The TEM images in Fig. S11 show that the NW morphology is well retained and Ti-rich shell becomes more obvious compared with the pristine NW. We further examine the NW through STEM combined with EELS spectrum. EELS line scan was collected at different positions from bulk to surface as shown in Fig. S12a. By integrating the intensity of O, Ti, and Mn peaks, the relative composition can be obtained in Fig. S12c. Interestingly, O K edge pre-peak intensities are quite low on both surface sides. The reduced ratio of the O K edge pre-peak intensities to the main peak can result from a change in the local environment of oxygen, especially from the oxygen vacancies formed on the surface. The relative distribution of chemical composition of Mn, Ti, and O elements are plotted in Fig. S12c. The oxygen ratio shows the same trend and gradually increases from 39% in the surface and become stabilized at ~43% from 10 nm towards the middle area. The lowered oxygen ration in the surface suggests the formation of oxygen vacancy. The trend is similar to the pristine NW, suggesting that the oxygen vacancies as well as the concentration gradient structure retained in the NW body. We further did the *ex-situ* XPS spectrum to investigate the valence state of Mn and Ti during cycling in Fig. S13. It is found that there is no obvious shift of Ti 2p spectrum during the cycling in Fig. S13c. On contrast, Mn 2p spectrum shift towards low binding energy during discharging while high binding energy upon charging. These results suggest that the redox center in the electrochemical reaction took place in Mn rather than Ti.

To gain a better insight into the physical origin of improved kinetics in both H^+ and Zn^{2+} storage, we conducted DFT calculations in Fig. 4 to investigate the charge density distribution around oxygen vacancy. The Ti substitution and its derived oxygen vacancy create a charge depletion zone and finally form a built-in electric field. The unbalanced charge and spin distribution in the tunnel induce an interfacial electric-field within the interfaces, while lopsided charge distribution around Ti substitution site and its derived oxygen vacancies resulted in a local in-plane electric-field, open the [MnO_6] octahedral walls, thus promoting ion diffusion/electron transport (Fig. 4e). On the atomic level, upon charging, the electron-dense area around the vacancy would attract ions due to the Coulomb attractive force, which accelerate the ion diffusion in the bulk. When fully charged, the electron-dense area will tend to be electrically neutral. In this regard, upon charging, the secondary electric field induced by the vacancy will facilitate ion migration. In this way the much lower charge-transfer impedance and diffusion rate of Zn^{2+} and H^+ in Fig. 4a, and 4b is achieved, facilitating the both Zn^{2+} and H^+ intercalation in the tunnel [44,51,52].

3. Conclusion

In summary, we have experimentally introduced of oxygen defect through gradient Ti doping in MnO_2 NWs as a high-performance cathode material for zinc battery. In this system, the surface gradient Ti substitution in MnO_2 NWs creates oxygen vacancy and opens the [MnO_6] octahedral walls. In this way, the Ti substitution and its derived the oxygen vacancy will induce a built-in electric field in the tunnel of α-MnO_2, which could accelerate ion/electron migration rates, leading to high rate performance for zinc battery. Profiting from the Ti substitution and oxygen vacancies, both diffusion coefficients and charge transfer resistances of Zn^{2+} and H^+ ions in Ti−MnO_2 NWs are improved, leading to a high-rate and long-life Zn/MnO_2 battery. More significantly, the strategy of optimizing by tuning the ion/electron migration behavior proposed in this work could provide a feasible design and doping strategy for developing other electrodes for multivalent-ion battery.

Competing financial interests

The authors declare no competing financial interests.

Acknowledgements

This work was supported by the National Key Research and Development Program of China (2016YFA0202603), the Programme of Introducing Talents of Discipline to Universities (B17034), the National Natural Science Foundation of China (51521001 and 51602239), the National Natural Science Fund for Distinguished Young Scholars (51425204), the National Students Innovation and Entrepreneurship Training Program (WUT: 20181049701037), and the Hubei Provincial Natural Science Foundation of China (2016CFB267).

Appendix A. Supplementary data

Supplementary data to this article can be found online at https://doi.org/10.1016/j.nanoen.2019.04.038.

References

[1] J. Zhi, A.Z. Yazdi, G. Valappil, J. Haime, P. Chen, Science Advances 3 (2017) e1701010.
[2] K. Zhao, M. Wen, Y. Dong, L. Zhang, M. Yan, W. Xu, C. Niu, L. Zhou, Q. Wei, W. Ren, X. Wang, L. Mai, Advanced Energy Materials 7 (2017) 1601582.
[3] K. Zhao, F. Liu, C. Niu, W. Xu, Y. Dong, L. Zhang, S. Xie, M. Yan, Q. Wei, D. Zhao, L. Mai, Advanced Science 2 (2015) 1500154.
[4] K. Zhao, L. Zhang, R. Xia, Y. Dong, W. Xu, C. Niu, L. He, M. Yan, L. Qu, L. Mai, Small 12 (2016) 588.
[5] B. Xu, C.R. Fell, M. Chi, Y.S. Meng, Energy Environ. Sci. 4 (2011) 2223.
[6] W. Xu, S. Dai, G. Liu, Y. Xi, C. Hu, X. Wang, Electrochim. Acta 203 (2016) 1.
[7] W. Xu, Z. Jiang, Q. Yang, W. Huo, M.S. Javed, Y. Li, L. Huang, X. Gu, C. Hu, Nanomater. Energy 43 (2018) 168.
[8] H. Tang, Z. Peng, L. Wu, F. Xiong, C. Pei, Q. An, L. Mai, Electrochemical Energy Reviews 1 (2018) 169.
[9] J. Lu, Z. Chen, F. Pan, Y. Cui, K. Amine, Electrochemical Energy Reviews 1 (2018) 35.
[10] M.A. Khan, H. Zhao, W. Zou, Z. Chen, W. Cao, J. Fang, J. Xu, L. Zhang, J. Zhang, Electrochemical Energy Reviews 1 (2018) 483.
[11] C. Zhu, R. Usiskin, Y. Yu, J. Maier, Science 358 (2017) 1400.
[12] H. Zhou, H. Cheng, H. Zhao, K. Zhao, Y. Zhao, J. Zhang, Q. Xu, X. Lu, J. Electrochem. Soc. 166 (2019) A59.
[13] J.F. Parker, C.N. Chervin, I.R. Pala, M. Machler, M.F. Burz, J.W. Long, D.R. Rolison, Science 28 (2017) 415.
[14] L. Dong, X. Ma, Y. Li, L. Zhao, W. Liu, J. Cheng, C. Xu, B. Li, Q.-H. Yang, F. Kang, Energy Storage Materials 13 (2018) 96.
[15] X. Xu, A. Enaiet Allah, C. Wang, H. Tan, A.A. Farghali, M. Hamdy Khedr, V. Malgras, T. Yang, Y. Yamauchi, Chem. Eng. J. 362 (2019) 887.
[16] X. Xu, H. Tan, Z. Wang, C. Wang, L. Pan, Y.V. Kaneti, T. Yang, Y. Yamauchi, Environ. Sci. Nano 6 (2019) 981.
[17] K. Wu, K. Du, G. Hu, J. Mater. Chem. 6 (2018) 3444.
[18] K. Wu, K. Du, G. Hu, J. Mater. Chem. 6 (2018) 1057.
[19] K. Wu, H. Yang, L. Jia, Y. Pan, Y. Hao, K. Zhang, K. Du, G. Hu, Green Chem. 21 (2019) 1472.
[20] Y. Cai, F. Liu, Z. Luo, G. Fang, J. Zhou, A. Pan, S. Liang, Energy Storage Materials 13 (2018) 168.
[21] P. He, G. Zhang, X. Liao, M. Yan, X. Xu, Q. An, J. Liu, L. Mai, Advanced Energy Materials (2018) 1702463.
[22] P. Hu, T. Zhu, X. Wang, X. Wei, M. Yan, J. Li, W. Luo, W. Yang, W. Zhang, L. Zhou, Z. Zhou, L. Mai, Nano Lett. 18 (2018) 1758.
[23] D. Kundu, B.D. Adams, V. Duffort, H. Vajargah, L.F. Nazar, Nature Energy 1 (2016) 16119.
[24] H. Pan, Y. Shao, P. Yan, Y. Cheng, K.S. Han, Z. Nie, C. Wang, J. Yang, X. Li, P. Bhattacharya, K.T. Mueller, J. Liu, Nature Energy 1 (2016) 16039.
[25] C. Xia, J. Guo, Y. Lei, H. Liang, C. Zhao, H.N. Alshareef, Adv. Mater. 30 (2018) 1705580.
[26] C. Xia, J. Guo, P. Li, X. Zhang, H.N. Alshareef, Angew. Chem. Int. Ed. 57 (2018) 3943.
[27] C. Xu, B. Li, H. Du, F. Kang, Angew. Chem. Int. Ed. 51 (2012) 933.
[28] M. Yan, P. He, Y. Chen, S. Wang, Q. Wei, K. Zhao, X. Xu, Q. An, Y. Shuang, Y. Shao, K.T. Mueller, L. Mai, J. Liu, J. Yang, Adv. Mater. 30 (2018) 1703725.
[29] N. Zhang, F. Cheng, J. Liu, L. Wang, X. Long, X. Liu, F. Li, J. Chen, Nat. Commun. 8 (2017).
[30] Q. Zhao, W. Huang, Z. Luo, L. Liu, Y. Lu, Y. Li, L. Li, J. Hu, H. Ma, J. Chen, Science Advances 4 (2018) eaao1761.
[31] W. Sun, F. Wang, S. Hou, C. Yang, X. Fan, Z. Ma, T. Gao, F. Han, R. Hu, M. Zhu, C. Wang, J. Am. Chem. Soc. 139 (2017) 9775.
[32] V. Soundharrajan, B. Sambandam, S. Kim, M.H. Alfaruqi, D.Y. Putro, J. Jo, S. Kim, V. Mathew, Y.-K. Sun, J. Kim, Nano Lett. 18 (2018) 2402.
[33] Q. Pang, C. Sun, Y. Yu, K. Zhao, Z. Zhang, P.M. Voyles, G. Chen, Y. Wei, X. Wang, Advanced Energy Materials (2018) 1800144.
[34] N. Zhang, Y. Dong, M. Jia, X. Bian, Y. Wang, M. Qiu, J. Xu, Y. Liu, L. Jiao, F. Cheng, ACS Energy Letters (2018) 1366.
[35] L. Zhang, L. Chen, X. Zhou, Z. Liu, Advanced Energy Materials 5 (2014) 1400930.
[36] T. Xiong, Z.G. Yu, H. Wu, Y. Du, Q. Xie, J. Chen, Y.-W. Zhang, S.J. Pennycook, W.S.V. Lee, J. Xue, Adv. Energy Mater. (2019) 1803815.
[37] J. Jeong, N. Aetukuri, T. Graf, T.D. Schladt, M.G. Samant, S.S.P. Parkin, Science 339 (2013) 1402.
[38] Y. Liu, T. Zhou, Y. Zheng, Z. He, C. Xiao, W.K. Pang, W. Tong, Y. Zou, B. Pan, Z. Guo, Y. Xie, ACS Nano 11 (2017) 8519.
[39] C. Yan, Y. Zhu, Y. Li, Z. Fang, L. Peng, X. Zhou, G. Chen, G. Yu, Adv. Funct. Mater. 28 (2018) 1705951.
[40] Y. Zheng, T. Zhou, X. Zhao, W.K. Pang, H. Gao, S. Li, Z. Zhou, H. Liu, Z. Guo, Adv. Mater. 29 (2017) 1700396.
[41] H. Zhang, Y. Jiang, Z. Qi, X. Zhong, Y. Yu, Energy Storage Materials 12 (2018) 37.
[42] P. Lu, Y. Sun, H. Xiang, X. Liang, Y. Yu, Advanced Energy Materials 8 (2018) 1702434.
[43] T. Koketsu, J. Ma, B.J. Morgan, M. Body, C. Legein, W. Dachraoui, M. Giannini, A. Demortière, M. Salanne, F. Dardoize, H. Groult, O.J. Borkiewicz, K.W. Chapman, P. Strasser, D. Dambournet, Nat. Mater. 16 (2017) 1142.
[44] W. Li, D. Corradini, M. Body, C. Legein, M. Salanne, J. Ma, K.W. Chapman, P.J. Chupas, A.-L. Rollet, C. Julien, K. Zhagib, M. Duttine, A. Demourgues, H. Groult, D. Dambournet, Chem. Mater. 27 (2015) 5014.
[45] L. Wu, F. Xu, Y. Zhu, A.B. Brady, J. Huang, J.L. Durham, E. Dooryhee, A.C. Marschilok, E.S. Takeuchi, K.J. Takeuchi, ACS Nano 9 (2015) 8430.
[46] H.-R. Yao, P.-F. Wang, Y. Gong, J. Zhang, X. Yu, L. Gu, C. OuYang, Y.-X. Yin, E. Hu, X.-Q. Yang, E. Stavitski, Y.-G. Guo, L.-J. Wan, J. Am. Chem. Soc. 139 (2017) 8440.
[47] Y. Wang, J. Liu, B. Lee, R. Qiao, Z. Yang, S. Xu, X. Yu, L. Gu, Y.-S. Hu, W. Yang, K. Kang, H. Li, X.-Q. Yang, L. Chen, X. Huang, Nat. Commun. 6 (2015).
[48] Y. Yuan, C. Liu, B.W. Byles, W. Yao, B. Song, M. Cheng, Z. Huang, K. Amine, E. Pomerantseva, R. Shahbazian-Yassar, J. Lu, Joule 3 (2018) 1.
[49] L. Xu, Q. Jiang, Z. Xiao, X. Li, J. Huo, S. Wang, L. Dai, Angew. Chem. Int. Ed. 55 (2016) 5277.
[50] L.-K. Wu, H. Wu, H.-B. Zhang, H.-Z. Cao, G.-Y. Hou, Y.-P. Tang, G.-Q. Zheng, Chem. Eng. J. 334 (2018) 1808.
[51] H. Huang, B. Dai, W. Wang, C. Lu, J. Kou, Y. Ni, L. Wang, Z. Xu, Nano Lett. 17 (2017) 3803.
[52] T.C. Kaspar, D.K. Schreiber, S.R. Spurgeon, M.E. McBriarty, G.M. Carroll, D.R. Gamelin, S.A. Chambers, Adv. Mater. 28 (2016) 1616.